Developments towards an ELM-free pedestal radiative cooling scenario using noble gas seeding in ASDEX Upgrade

A. Kallenbach, M. Bernert, P. David, M. Dunne, R. Dux, E. Fable, R. Fischer, L. Gil[1], T. Görler, F. Janky, R.M. McDermott, W. Suttrop, G. Tardini, M. Wischmeier, ASDEX Upgrade Team[2], EUROfusion MST1 team[3]

Max Planck Institute for Plasma Physics, D-85748 Garching, Germany
[1]Instituto de Plasmas e Fusao Nuclear, IST, Unversidade de Lisboa, Portugal
[2]H. Meyer et al., 2019 Nucl. Fusion **59** 112014
[3]B. Labit et al., 2019 Nucl. Fusion **59** 086020

Abstract. Integrated edge-localized-mode (ELM)-free or small ELM scenarios for DEMO are investigated in ASDEX Upgrade using argon seeding for radiative power removal mainly in the pedestal region. An important aspect is the modification of the electron pressure in the pedestal by the additional radiative power losses. Full ELM suppression could be achieved in a no-ELM H-mode scenario featuring an edge electromagnetic quasicoherent mode up to a heating power of 5 MW, where argon radiation allowed the extension of the heating power operational space. At higher powers up to 12 MW (reaching the beta limit), ELMs of reduced size prevail and detachment is obtained by the argon seeding. Control of the position of a radiating zone localized inside the X-point was found to be favorable compared to the control of the separatrix power for low P_{sep}/P_{heat}. Integration of pedestal cooling with Ar and ELM suppression by resonant magnetic perturbations (RMP) allowed an increase of the core radiation and a partial recovery of normalized confinement to H_{98}=1. This favorable behaviour is finally limited by the loss of the RMP density pump-out effect, followed by an ELM-free H-mode phase and re-occurrence of ELMs. For an active tailoring of the pedestal pressure profile, precise knowledge of the radiation profile is required. Modelling of the argon radiation profile with the STRAHL code showed good agreement with bolometry only if charge exchange of neutral deuterium with argon ions was taken into account, highlighting the importance of the neutral density in the pedestal region. In view of best integration of a no-ELM scenario with divertor detachment and high heating power, the divertor compression and enrichment of argon and neon were compared using dynamic gas puff experiments. Argon shows more than a factor of 3 higher divertor enrichment compared to neon, but the absolute values decrease with higher neutral deuterium pressure.

1. Introduction

Due to the limited power exhaust capability of the divertor, a future DEMO reactor needs a substantial core/pedestal radiation level, controlled and tailored by an appropriate seed impurity mix [1] [2]. The core/pedestal seeding has to be integrated with substantial divertor radiative cooling and a no/very small ELM plasma regime [3] [4] [5]. In fact, the requirement to avoid ELMs is expected to be more strict in DEMO compared to ITER [6] due to higher DEMO neutron and plasma fluences. Sufficient energy confinement and low fuel dilution are required boundary conditions of the seeding scenario. Operation in H-mode requires a separatrix power, P_{sep}, above 150 MW in DEMO. A major fraction of the power crossing the separatrix needs to be radiated in the divertor in order to facilitate detachment. Using the parallel heatflux as a measure for the difficulty to achieve detachment, depending on the model for the heat flux width, P_{sep}/R or $P_{sep}B/R$ are often taken as proxies for this difficulty (at fixed density). Detachment by impurity seeding is easier achieved at higher density and the former expressions change when an upper limit for the separatrix density is built in [7]. Nevertheless, for approaching as similar as possible conditions to DEMO, divertor radiation experiments in present devices should be done at the highest possible P_{sep} values.

Taking into account the radiative capabilities of the potential seeding species (N_2, Ne, Ar, Kr, Xe), only Ar is expected to contribute substantially to both pedestal and divertor radiation for reactor conditions [8]. Independent control of core and divertor radiation with different seeding species was successfully demonstrated in ASDEX Upgrade for partially detached divertor conditions [9], which is the foreseen ITER scenario. Even more sophisticated radiation control may be required for DEMO to cope with the need to avoid ELMs. This means either the integration of a pedestal radiative scenario with a no-ELM regime, or the use of a regime with strong radiation inside the X-point, which may lead to ELM suppression by itself, as observed in the X-point radiator scenario [10]. Independent of the scenario finally chosen, tailoring of the pedestal pressure profile by strong radiation has to be regarded as an important actuator for the achievement of a MHD-stable pedestal. The present study is complementary to investigations of the small ELM scenario [11] in highly shaped, near double null configurations, where additional pedestal losses are provided by ballooning modes close inside the separatrix.

This paper reports on ASDEX Upgrade experiments with argon seeding aiming at mitigation or full suppression of ELMs. Section 2 describes ASDEX Upgrade experiments with argon seeding into different ELMy H-mode and no-ELM discharge scenarios. The effect of argon radiation on pedestal, confinement and stability is discussed in section 3. High impurity enrichment in the divertor is a necessary condition for efficient divertor radiative power exhaust. The divertor enrichment of relevant impurities is investigated in section 4. Section 5 summarizes the main findings.

2. Experiments with argon seeding

Argon is the most suitable species for the study of the combination of pedestal and divertor radiative cooling due to its high values of the radiative loss function L_z for electron temperatures of a few 100 eV [12], in combination with high values for typical divertor temperatures. Due to its strong radiation inside the separatrix, the reaction of the divertor radiation to the Ar injection is often masked by a strong reduction of the power entering the divertor for typical ASDEX Upgrade conditions. Therefore, the current study concentrates on the radiation in the main plasma. A combination with divertor radiative cooling for partial detachment, either by Ar or a different species, is not expected to be an issue as it was successfully demonstrated in double-feedback experiments on ASDEX Upgrade [9]. Nevertheless, the enrichment of the different impurities in the divertor needs to be considered for reactor scenarios due to their impact on the burn rate via fuel dilution [13].

2.1. Different plasma states during argon seeding

With increasing argon seeding level, ASDEX Upgrade H-mode plasmas develop through a number of different stages, which can be individually controlled by different feedback procedures. Figure 1 shows time traces of a discharge where the separatrix power is

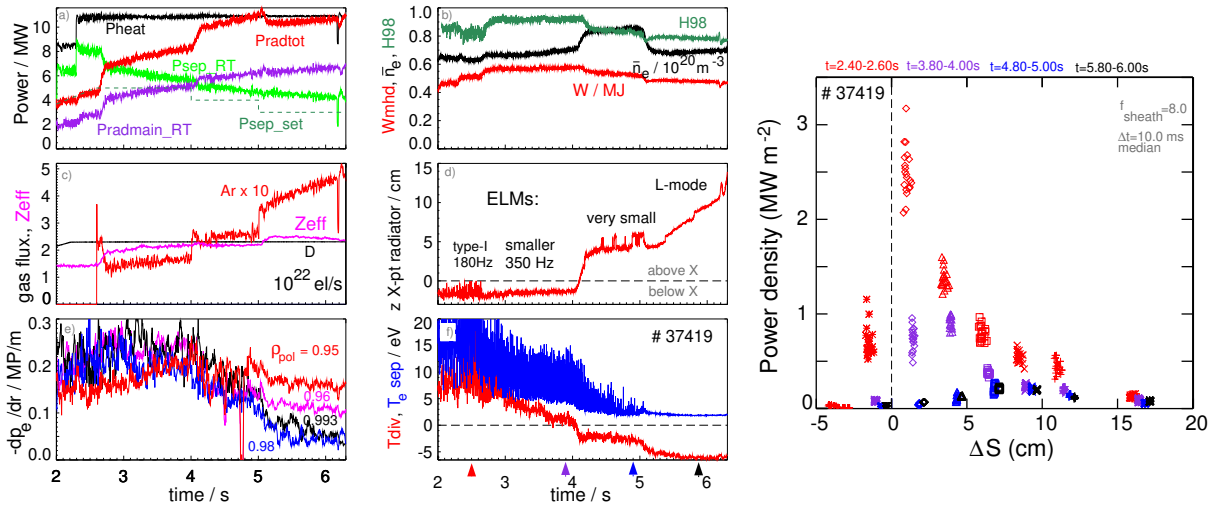

Figure 1. *left: time traces of a discharge with increasing Ar seeding level by Psep feedback control. a) heating and radiated power, b) stored energy, H_{98} confinement qualifier and line-averaged density, c) D and Ar valve flux and Z_{eff}, d) vertical position of the highly radiating zone relative to the X-point, e) electron pressure gradient from integrated data analysis for different ρ_{pol} in the pedestal region, f) electron temperature from a triple probe in the SOL close to the outer strike point and Tdiv global divertor temperature indicator [14]. right: heat flux profiles from LPs for different time points.*

continuously reduced by argon seeding via real time feedback on P_{sep}= P_{heat}-$P_{rad,main}$ [9]. The discharge has significant D puffing, which means that the confinement quality is reduced compared to low-fueling cases due to a higher separatrix density [15], but

the corresponding divertor pressure [16] of $p_{0,div} \approx 1.5$ Pa allows detachment with Ar as the only seeding species. With the onset of the Ar puff at t= 2.6 s, the ELM frequency increases and the normalized total energy loss per ELM decreases from 5 to 2 %. At 4 s, the radiation zone moves from the divertor into the confined region close to the X-point, see fig. 1d. Pedestal and line averaged density rise, the stored energy is slightly reduced, and the divertor detaches. This behaviour is very similar to the pronounced detachment observed with nitrogen seeding [12]. There are still high-frequency ELMs, but with 1 % or less relative energy loss. Figure 1e shows the local electron pressure gradient in the pedestal region. At the intermediate Ar radiation level, the pressure gradient at ρ_{pol}=0.98 starts to decrease, while a slight rise is seen further in at ρ_{pol}=0.95. This behaviour is qualitatively similar to that of highly shaped plasmas described below. With further reduced P_{sep}, after 5 s the pressure gradient close to the separatrix collapses and the discharge enters L-mode albeit maintaining a high gradient further inside and an improved H_{98} factor of about 0.8. Finally, the radiating zone moves further upward, deeper into the confinement zone, and a disruption terminates the pulse.

2.2. Ar injection into intrinsically ELM-free and close-to ELM free scenarios

While Ar pedestal radiation (Kr and Xe are other candidates for DEMO [5]) is an important tool for the required reduction of P_{sep} it needs to be integrated into a no-ELM scenario which is considered a required condition for DEMO. A successful example is shown in the left part of figure 2, where an ELM free H-mode phase is maintained at 5 MW mixed NBI/ECRH heating power. This ELM-free H-mode regime recently discovered in ASDEX Upgrade [17] exhibits similarities to the Alcator C-mod EDA H-mode [18]. ELM suppression is in this case likely related to an electromagnetic quasicoherent mode causing enhanced transport losses and thus leading to a stable pedestal. A spectrogram of the edge DCN interferometer channel shows the quasicoherent mode in figure 3, the mode terminates when the heating power is stepped down. The presence of Ar radiation, causing additional power loss in the pedestal, extended the existence of this no-ELM regime to higher heating powers.

The separatrix power of # 36330 is below $P_{LH} \approx 3$ MW predicted by the Martin scaling [19], but the major fraction of the radiation is emitted in the pedestal with the peak between ρ_{pol}= 0.98-0.99. The experimental L-H transition occurs at lower density around 1.2 MW in these shots. The higher power discharge shown in the right panel comes close to the global parameter range expected for DEMO conditions ($H_{98} \approx 1.2$, $\beta_N \leq 3$, triangularity δ= 0.42), with the maximum heating power / β_N possible without strong NTM activity and with partial outer divertor detachment between ELMs. There is no quaisicoherent mode present in this pulse and ELM suppression is not maintained despite the relatively high Ar seeding rate. Compared to a reference pulse without Ar seeding, energy confinement is improved and the ELM size reduced by about a factor 2. The discharge # 36330 with ELM suppression is fully attached during this phase

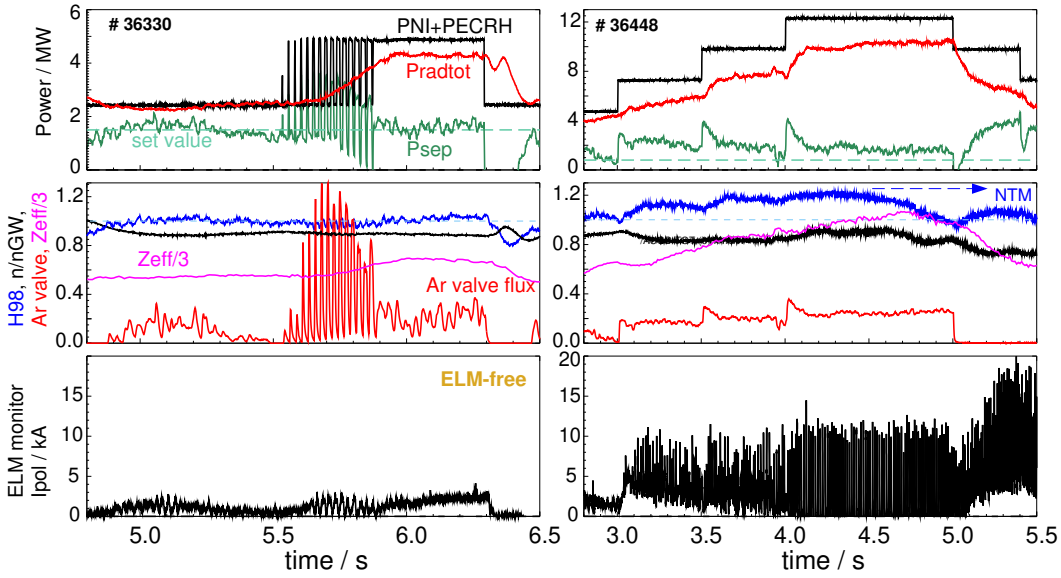

Figure 2. *Time traces of an ELM-free H-mode with Ar seeding at medium heating (left) and a corresponding high power discharge with reduced size ELMs remaining (right). Top: Heating power, total radiated power and power through separatrix, mid: Ar valve flux, H98-factor, density Greenwald fraction and line-averaged Z_{eff}, bottom: SOL divertor current as ELM monitor. I_p= 0.8 MA, q_{95}= 4.9, average triangularity δ= 0.42. Both discharges with P_{sep}= P_{heat}-$P_{rad,main}$ control [9].*

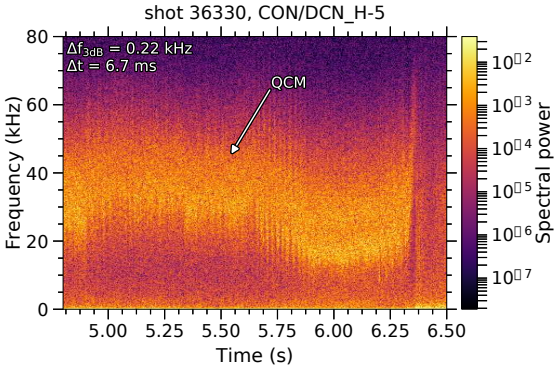

Figure 3. *Spectrogram of the edge interferometer chord showing the quasicoherent mode for the discharge from figure 2.*

with a peak heat flux derived from Langmuir probes of 5-10 MW/m^2. The higher power discharge # 36448 has a colder divertor plasma and is partially detached between ELMs with an inter-ELM peak heat flux around 1 MW/m^2. The reason for the different detachment behaviour of both discharges is not fully clear, the attached case has a slightly lower divertor neutral pressure (0.25 Pa vs. 0.3 Pa), another contributor may be the fact that we compare an inter-ELM phase with the time-average of an ELM-free phase.

No attempts were made so far to combine Ar seeding with the QH-mode [20]. The reason is that full ELM suppression could not be obtained in this scenario with W wall

[21], in contrast to earlier experiments with a C wall [22].

Alcator C-Mod experiments were not successful in demonstrating compatibility of the I-mode regime with divertor detachment [23]. These investigations are being continued in AUG [24].

2.3. Ar injection with X-point radiator regime

Another scenario with complete suppression of ELMs, albeit at somewhat reduced energy confinement, is the X-point radiator scenario which was in ASDEX Upgrade developed originally with nitrogen seeding [25], but is also observed with neon in EAST [26] and with nitrogen and neon in JET [27] [28]. This regime starts at partial divertor detachment and extends towards pronounced or even complete detachment with increasing vertical distance of the radiating zone relative to the X-point, thus deeper penetration of the radiating zone. Depending on penetration depth of the X-point radiator, full suppression of ELMs was obtained in AUG and JET [29], with energy confinement slightly lower compared to standard H-mode conditions. Recently,

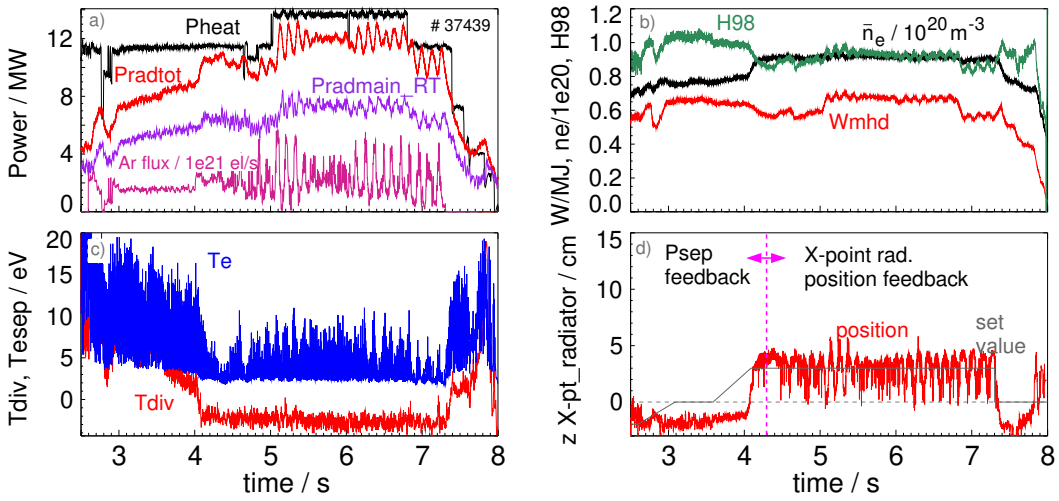

Figure 4. *Time traces of discharge with Ar seeding first by P_{sep}= P_{heat}-$P_{rad,main}$ feedback to establish an X-point radiator, from 4.3 s feedback of the radiator position. I_p= 0.8 MA. Z_{eff}= 2.0 in the seeded phase.*

a controller for the vertical position of the radiating zone has been developed on ASDEX Upgrade [10]. Such a controller is particularly useful for high main chamber radiation levels as obtained by Ar seeding in AUG and also foreseen for DEMO, since a P_{sep} feedback on the difference of heating power and main chamber radiation is not well conditioned if both quantities are similar in value and bear uncertainties. Figure 4 shows time traces of a discharge in which an X-point radiator was produced by P_{sep} feedback with Ar first, and at t= 4.3 s switched to feedback on the position of the X-point [10] [26]. A larger distance to the X-point here relates to a higher Ar puff rate. The radiator position is controlled quite well with quite dynamic actuator operation. During the phase with the radiator about 3 cm above the X-point, the divertor conditions are

between partial and pronounced detachment, with $T_e \approx 3$ eV at the strike point and time-averaged peak power load of 0.5 MW/m^2. ELMs are still present in this phase, with a frequency of about 180 Hz and a relative stored energy drop around 1.5 %.

2.4. Ar injection into resonant magnetic perturbation (RMP) ELM-suppressed H-modes

First attempts to integrate pedestal radiative power removal with RMP ELM-suppressed H-modes [30] [31] revealed challenges as well as possible prospects, as shown in figure 5. The pulse had a consecutive chain of Ar puffs with increasing duration into an RMP ELM-suppressed phase. Z_{eff} rises only moderately due to the Ar puff, which is explained by a reduction of the boron and tungsten densities, as monitored by the SPRED spectrometer and CXRS on boron (not shown). The Z_{eff} contribution of Ar^{16} measured by CXRS [32] at ρ_{pol}= 0.7 (figure 5c) shows an increase during the puff chain up to dZ_{eff}= 0.55 during the ELM-suppressed phase. The normalized energy

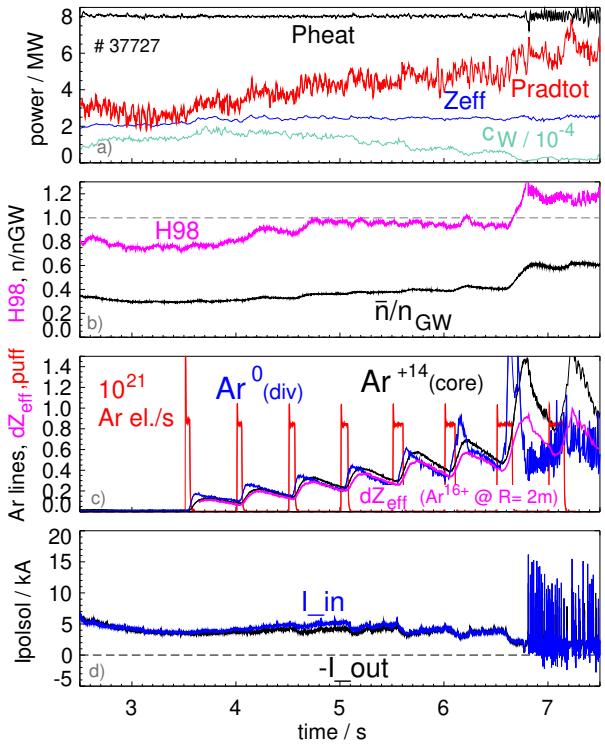

Figure 5. *Time traces of discharge with Ar pulses from the outer midplane into an RMP ELM-suppressed H-mode. a) heating power, total radiation, Z_{eff} and core tungsten concentration, b) H_{98} and Greenwald density fraction, c) Ar puff rate and spectral line intensities from core (SPRED VUV spectrometer) and visible spectroscopy in the outer divertor. Also shown is the contribution of Ar^{16+} from CXRS measurements at R=2 m / ρ_{pol}= 0.7, where this ionisation stage dominates. d) inner and outer SOL current (ELM monitor). B-coils set for ELM suppression throughout the time interval shown. Divertor pressure $p_0 \leq 0.1$ Pa. The tungsten concentration in the plasma decreases from 1.5 10^{-4} to 6 10^{-5} during the Ar puff.*

confinement gradually improves during the first part of the Ar injection, as does the plasma density. The Ar content in the main chamber as well as in the divertor exhibits step-wise increases due to the relatively weak divertor pumping rate (low divertor neutral pressure, see next section 4). At t= 6.6 s, the pump-out mechanism is lost, leading to an ELM-free H-mode phase with a strong rise of density and stored energy, until ELMs finally reappear at t=6.8 s. Reasons for the loss of pump-out may be a slight increase of density, Z_{eff} or a subtle change in edge rotation [31] [33]. Increased radiative losses inside the separatrix may also play a role. The moderate rise of Z_{eff} and the behaviour of Ar spectral lines in the core and divertor suggest no particularly unfavorable transport behaviour of Ar in the pedestal due to the absence of ELMs, as suggested by previous experiments with W injection [31]. The faster rise of the neutral Ar signal in the divertor compared to the He-like Ar^{16+} in the outer core indicates a fast transport of the Ar atoms puffed in the outer midplane towards the divertor also during the ELM suppressed phase. However, the decay time of the Ar^{16+} after each pulse is clearly longer in comparison to the ELMy phase after 6.8 s suggesting an increased Ar core confinement time under ELM-suppressed conditions and/or a reduced pumping efficiency. Recent helium exhaust experiments comparing RMP ELM-suppressed and non-perturbed ELM H-modes in DIII-D showed a better global exhaust of helium with RMPs [34]. A caveat of the present scenario regarding radiative power exhaust is the low density required for ELM suppression [31], which reduces the radiated power per Ar ion in the core and divertor and also leads to slow pumping, challenging active control. If the restriction to low densities for RMP ELM suppression turns out to be absent in devices like ITER and DEMO, efficient radiative power removal in the pedestal might be feasible.

3. Effect of argon radiation on pedestal, confinement and stability

Figure 6 shows the radiation profiles of the high power seeded discharge from figure 2 (right traces) from deconvolution of foil bolometry and STRAHL modelling of the dominant radiation contributors, Ar and W [35]. The STRAHL modelling exhibits a more localized emission in the pedestal region, which may be explained by limited spatial resolution of the deconvolution on the one hand and omitted (small) contributions of B and C in the STRAHL modelling on the other hand. The experimental radiation profile of a reference discharge without seeding is also shown, the total main chamber radiation level is about 4 MW lower compared to the Ar seeded case. Despite the considerable radiation inside the separatrix, the Ar core radiation does not lead to a degradation of energy confinement, and even to an improvement. In the case of figure 2, the normalized confinement H_{98} is increased from 1.1 in the reference discharge to 1.2 in the Ar seeded case, as shown in figure 6 (right). The confinement improvement is in this case situated inside the pedestal top as discussed below. H-mode confinement increase had been observed with medium-Z seeding in JET after-puff phases (Ne, Ar) [36], and in AUG with Ar and Kr [12]. In contrast, degradation of energy confinement at high Ar radiation levels was observed in Alcator C-Mod EDA H-modes [37], [38]. Ar

seeding into ELMing high performance DIII-D plasmas in double-null configuration (at low D fueling level) found issues with high fuel dilution and tearing mode activity [39].

The analysis of the plasma radiation during impurity seeding with the STRAHL code [35] revealed that the line-integrated bolometer measurements in the outer plasma region can only be reconciled if charge exchange with neutral deuterium is taken into account. Figure 7 shows an example for the shot introduced in figures 2(right) and 6. The enhancement of the Ar radiation in the pedestal region is caused by a shift of the Ar ionization balance towards lower stages. As a consequence, Li-like and lower Ar ionization stages, which are much more radiative compared to He-like argon, exhibit much higher concentrations in the pedestal region. This leads to an increase of the pedestal radiation by about a factor 3, see figure 7d). A similar increase due to charge exhange is observed for neon [35]. Corresponding effects are also predicted for ITER pedestal temperatures, where a slighty reduced enhancement is predicted for Kr and only a moderate rise for Xe [35]. The importance of this effect for DEMO will depend on the SOL opacity for neutrals, and the effect of neutrals released via pellets.

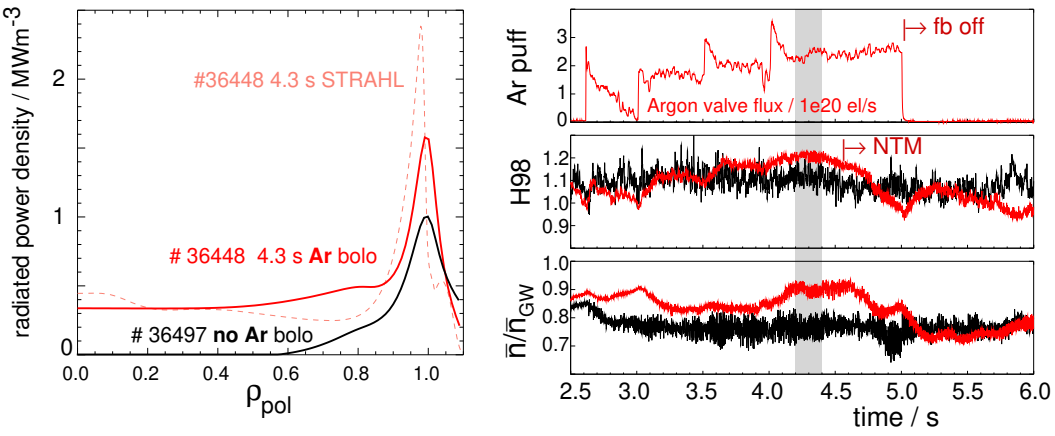

Figure 6. *left: Radiated power density from deconvolution of foil bolometry for the Ar seeded discharge and for comparison for a twin shot without Ar injection. The latter has a higher low-Z impurity content, but a lower central tungsten density. For the Ar seeded case, STRAHL modelling of the radiated power by Ar and W is also shown (see fig. 7. right: normalized energy confinement and density for the high power discharges with and without Ar seeding. The MHD resulting in confinement degradation in # 36448 after 4.5 s is a 1/1 mode, which briefly turns into 4/3 (higher frequency) and, finally, into 3/2. The shaded time interval is further analysed in the following figures.*

The most important effect of Ar radiation on the ELM behaviour is the reduction of the electron pressure in the pedestal region. This may, either on its own or in combination with MHD activity or turbulence, keep the edge stable against ELMs. The effect of Ar radiation may be a combination of local transport changes and possible density profile variations via SOL physics, which were found in stability analyses of nitrogen seeded plasmas where the stability boundary was shifted to higher pressure gradients [40]. When the argon radiation becomes too strong, the edge ion pressure may be reduced so far via electron-ion coupling that the neoclassical electric field well

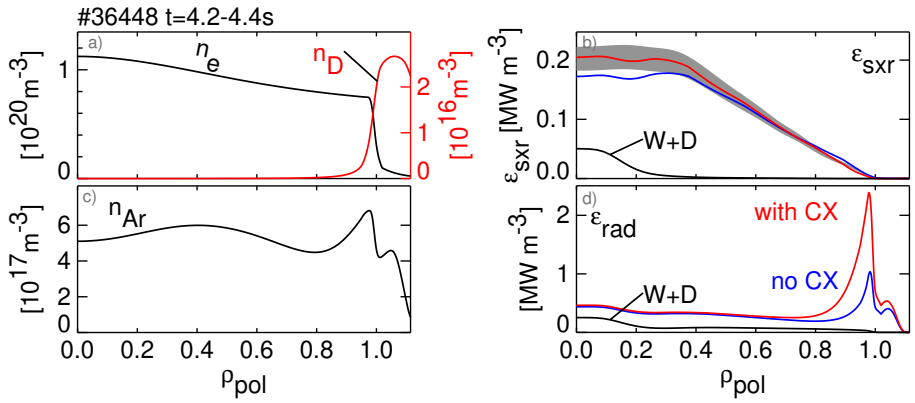

Figure 7. *Modelling of the radiation of # 36448 with the impurity transport code STRAHL. a) Experimental electron density and neutral D density from modelling, b) Experimental and modelled SXR-intensity, c) inferred Ar density profile, d) modelled radiated power density, including tungsten radiation. The total core radiation emitted inside the separatrix is 8 MW. Red lines take the charge exchange with D into account, blue lines are calculated without this effect.*

(proportional to the ion pressure gradient) falls below the empirical AUG threshold for the ExB velocity of about 6.7 km/s [41] and an H-L transition occurs.

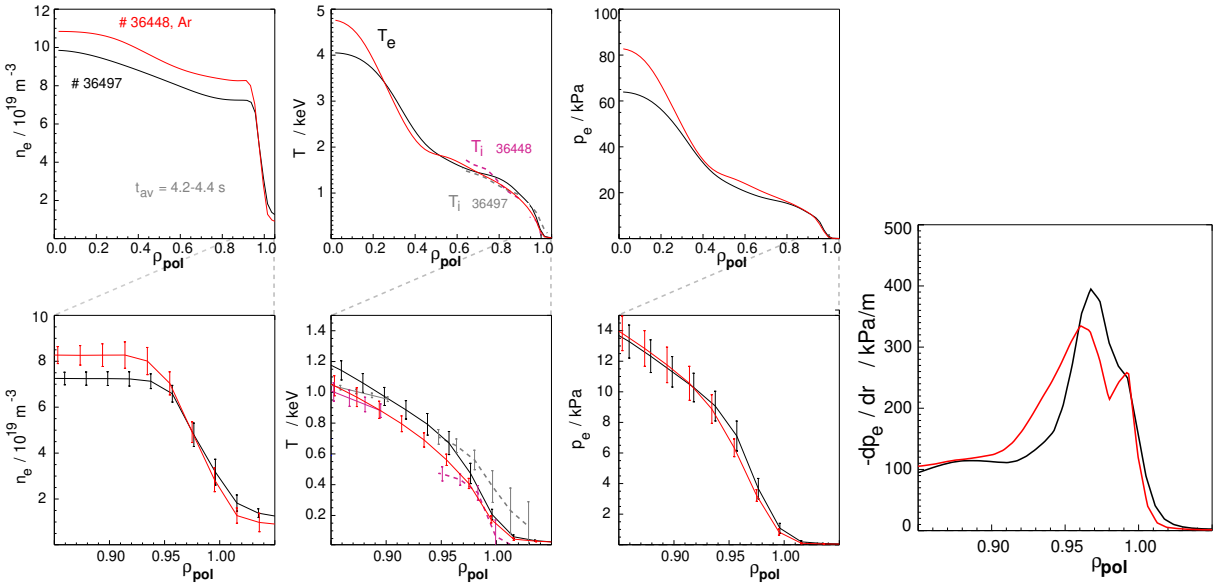

Figure 8. *Electron density, electron and B^{5+} ion temperature profiles, electron pressure and its radial gradient from the time interval of interest indicated in figure 6 for the discharge with strong Ar seeding and the no-Ar reference. Data are from integrated data analysis (n_e, T_e, p_e) and charge-exchange recombination spectroscopy [42].*

Electron density and temperature profiles from integrated data analysis [43] of various diagnostics are shown in figure 8 for the two pulses discussed above. The main effects of the Ar seeding are an increased electron density throughout the core

plasma, a reduced density in the SOL, thus a steeper electron density gradient in the pedestal, and a slightly reduced electron temperature gradient just inside the separatrix. Furthermore, T_e flattens a bit with Ar at half radius and steepens towards a higher value in the center. The edge ion temperature appears reduced with Ar seeding. The electron pressure gradient exhibits with Ar seeding a reduction very close to the separatrix, in line with the position of the Ar radiative layer, and an increase inside the pedestal top, suggesting a reduction of turbulence. This may be caused by a similar effect as observed in Ne seeded JET discharges [28], where ASTRA-TGLF simulations suggest a reduction of ITG turbulence due to main ion density dilution. The reduction of the ITG growth rate by increasing Z_{eff} had also been reported as explanation of the radiatively improved (RI) mode emerging from L-mode plasmas [44], where a peaking of the density profile is envolved. In the present H-mode studies, no bulk density profile peaking occurs, there is just an increase of the pedestal density. It has to be noted that the evaluation of the pressure gradient from measured density and temperatures underlies a significant level of uncertainty. However, since the reduction of the gradient (due to the effect on the temperature) close to the separatrix and the increase inside was observed consistently in a number of pulses (see figure 9d), the qualitative statement is regarded to be robust.

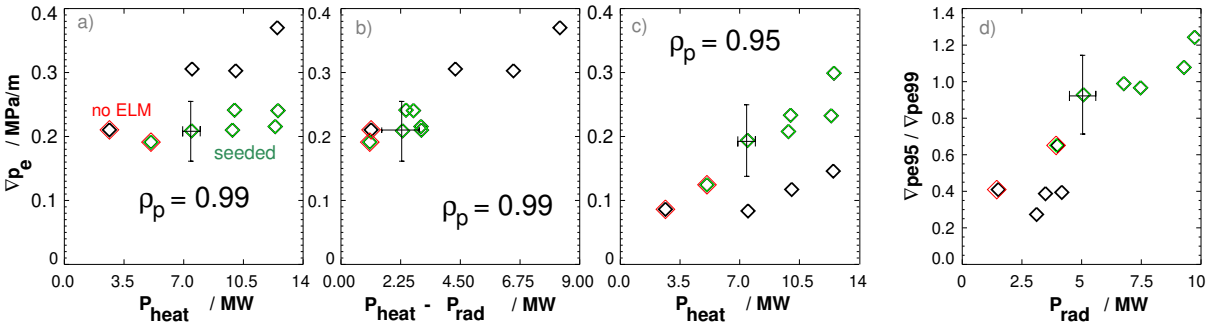

Figure 9. *Variation of the electron pressure gradient (real space outer midplane) derived from integrated data analysis with heating and main chamber radiated power which is dominated by Ar radiation in the seeded cases. a) pressure gradient at ρ_{pol}= 0.99 versus heating power, b) versus separatix power, c) pressure gradient at ρ_{pol}= 0.95 versus heating power and d) ratio of the electron pressure gradients at ρ_{pol}= 0.95 and ρ_{pol}= 0.99 versus main chamber radiated power. Data taken from flattop phases of discharges 36124, 36330, 36447, 36448, 36497 with same plasma current and (high) shaping.*

Figure 9 plots the electron pressure gradient for two locations, ρ_{pol}= 0.95 and ρ_{pol}= 0.99 for 10 steady state phases of 5 discharges with high shaping where the EDA-like no ELM regime is obtained at low power [17]. The peak radiation is expected between these locations. Therefore, the gradient at ρ_{pol}= 0.95 should be weakly effected by the radiative losses (but is obviously indirectly via transport). The pressure gradient at ρ_{pol}= 0.99 follows the local power flux, approximated by P_{heat}-P_{rad} closer than the heating power. The pressure gradient inside the pedestal, however, clearly rises with

the radiated power level. This can only be explained by transport effects. The ratio of the pressure gradients at ρ_{pol}= 0.95 and ρ_{pol}= 0.99 closely follows the radiated power (which is located mainly in the pedestal). Introduction of other radiating species, like Kr or Xe, may allow further tailoring of the pressure profile towards optimization of radiated power, core performance and ELM control.

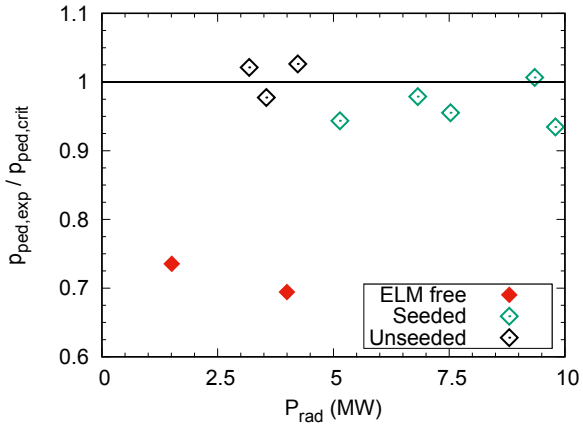

Figure 10. *Stability analysis of the discharge phases shown in figure 9 versus total radiated power. Good agreement of the ELMing phases with the calculated critical pressure is obtained, while the no-ELM phases are well in the stable range.*

Stability analysis against peeling-ballooning modes [40] of the shots of figure 9 is shown in figure 10. Very good agreement of the ELMing discharge phases with the critical pedestal pressure is obtained, while the two ELM-free phases are clearly below. There is no significant trend of the pedestal pressure with radiation, supporting the assumption that the improved confinement is caused by transport reduction further inward.

4. Integration with divertor detachment: impurity divertor enrichment

Finally, pedestal seeding needs to be integrated with detachment of a substantial power flux towards the divertor. This requires a high level of divertor radiation by a seed impurity, where the candidates for a standard, closed divertor are nitrogen, neon and argon. Nitrogen has the disadvantage of strong wall sticking and the formation of ammonia [45], which may lead to enhanced tritium inventories. An important parameter for the efficiency of a divertor seed impurity is the divertor compression or enrichment of the impurity [46]. A high divertor enrichment provides a high divertor radiation level combined with a low core fuel dilution. Finally, the impurity level in the divertor must match the detachment requirement, while simultaneously the pedestal radiator must be adjusted for the no-ELM condition.

In order to determine the seed impurity dynamics, and in particular the divertor enrichment, N, Ne and Ar puffs were injected into ELMy H-mode discharges with

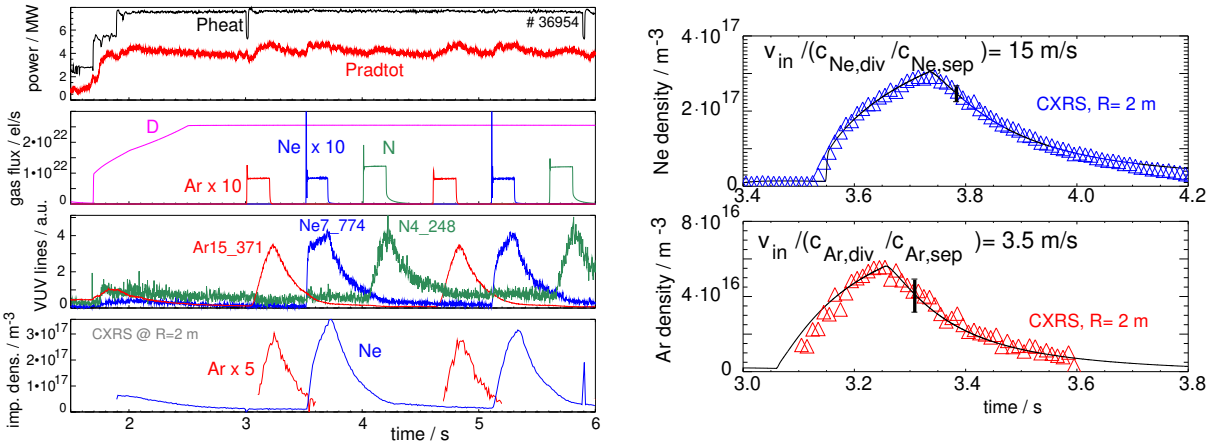

Figure 11. *left: time traces of a pulse with subsequent impurity puffs for model analysis. right panels: the full temporal evolution is fitted for Ne and Ar by variation of the parameter v_{in} / ($c_{z0,div}/c_{z,sep}$). A delay time of 30 ms (Ne) and 50 ms (Ar) has been used to match valve actuation and plasma response. I_p = 0.8 MA.*

different divertor neutral pressures. Figure 11 shows time traces of one discharge of the series. Analysis was performed with a simple multi-chamber particle balance model which allows essentially the determination of the divertor impurity enrichment. The model builds on previous work [47] [48] and provides a good description of the temporal development of impurity densities as well as steady state values measured by charge exchange recombination spectroscopy. The main plasma impurity source (ions/s) is described as $v_{in} c_{z,sep} n_{e,sep} A_{sep}$, where v_{in} is an effective inward pinch velocity (roughly understood as the radially averaged neoclassical inward pinch through the pedestal region), $c_z = n_z/n_e$ the upstream impurity concentration at the separatrix, A_{sep} the separatrix area (43 m^2 in AUG). The plasma impurity content is approximated by the impurity density measured by charge exchange recombination spectroscopy (CXRS) [49] at R=2 m (2/3 of the minor radius) and the plasma volume (13 m^3). For Ar the CXRS rate coefficients were obtained by a fit to Z_{eff}. The main plasma impurity confinement time τ_z is assumed constant at 0.08 s for the conditions considered here. A key element of the model is the relation of the upstream separatrix electron density $n_{e,sep}$ and the divertor neutral deuterium pressure p_0 measured in the divertor below the roof baffle, $n_{e,sep} = 2.65\ 10^{19}\ m^{-3}\ p_0^{0.31}$ [Pa] [16]. This relation is extended to the seed impurity with the neutral divertor atomic concentration $c_{z0,div} = p_{z,0}/(2p_0)$, while a possible divertor enrichment or de-enrichment of the impurity is described by the parameter $\eta_z = c_{z0,div}/c_{z,sep}$. The factor 2 in front of p_0 takes into account that deuterons are in molecular form at the location of the pressure measurement. The main plasma impurity source can be related to the neutral impurity concentration in the sub-divertor gas as $v_{in,z} c_{z0,div}/\eta_z\ n_{e,sep}\ A_{sep}$. Taking the neutral deuterium pressure from the experiment, and thus n_{sep} from the scaling, there is, for known pumping speed, only one free parameter left to determine the full temporal evolution of the impurity densities, namely $v_{in,z}/\eta_z$.

The measured decay rates of the core impurity densities and some results of the model are shown in figure 12. As most prominent and obvious result, a much higher divertor enrichment of Ar compared to Ne is derived for the whole neutral pressure range. The dominant uncertainty in the analysis is the pumping speed of the impurities, namely the degree of their entrainment in the D_2 flow. The error bar for Ar indicates the variation of the derived divertor enrichment when the entrainment factor is varied from no to full entrainment. A possible variation of the impurity confinement time τ_z, e.g. its shortening with increasing gas puff / neutral pressure [50], is compensated by adapting the parameters in the model, resulting in very little change of the derived enrichment values.

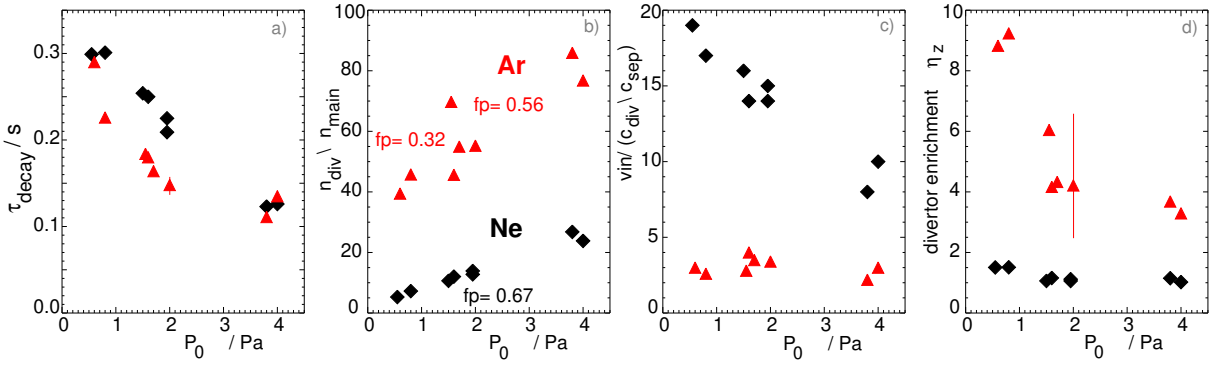

Figure 12. *a) measured impurity 1/e removal time from a fit to core Ne^{10+} and Ar^{16+} densities measured by CXRS , b) ratio of divertor neutral and core ion densities, fp indicating the the used pumping speed w.r.t D_2, c) fuelling parameter $v_{in}\, c_{z0,div}/c_{z,sep}$, d) divertor enrichment $c_{z,0,div}/c_{z,core}$, versus the neutral D_2 pressure measured below the roof baffle. b) and c) have been evaluated just at the stop time of the gas puff.*

The (pressure dependent) pumping speed for deuterium in the pump chamber is known from calibrations [51] and rises in the pressure range of this study (0.5 to 4 Pa below the roof baffle) from 140 to 230 m^3/s due to the effect of collisions between D_2 molecules. The effective D_2 pumping speed with respect to the region below the roof baffle, which is directly coupled to the divertor plasma, is limited by the conductance between roof baffle and pump chamber of 25 m^3/s, leading to a significant pressure drop by a factor of 4-6 towards the pump chamber. The pumping speed for noble gas atoms in the low pressure limit is expected to be lower by the thermal speed ratio corresponding to the square root of the mass ratio versus D molecules namely a factor 0.43 for Ne and 0.32 for Ar. Since some entrainment of Ne and Ar is obvious from the experimental removal rates, a geometric average between full and no entrainment is applied for higher pressure conditions, both for the conductance towards the pump chamber and to the cryopump itself, leading to relative pumping speeds w.r.t. to D_2 of 0.67 for Ne and 0.56 for Ar. Exact fitting would overstate the simple model used, but increased entrainment is clearly seen with rising D_2 pressure, as expected. The impurity pumping is the largest uncertainty source in the model used. The error bar in fig. 12c) shows the effect of the most extreme variation of the Ar entrainment in the pumped gas flow, namely no and

full entrainment. A variation of the core impurity confinement time τ_z showed only a very weak effect on the calculated enrichment, since it is compensated by a variation of the parameter $v_{in,z}/\eta_z$ in the model while fitting the measured impurity density. However, very large (i.e. factor 2) variations from the chosen fixed value τ_z =0.08 s lead to unrealistic density rise and decay times.

Monte Carlo calculations with realistic collision operators between Ar, Ne and D_2 and a realistic 3D divertor / pump chamber geometry would be highly desirable for a first-principle based description of impurity pumping [52]. Wall storage of Ne and Ar has been taken into account by a simple wall model. Wall storage determines the plasma densities of Ne and Ar in particular in the tail of the decay curve. In contrast, wall storage completely dominates the temporal behaviour of N under the present conditions, since N is far from stationarity due to its much higher wall saturation levels compared to the noble gases.

The modelling results shown in figure 12 allow a number of conclusions. The divertor compression, as shown in b), rises with D_2 pressure following the trend seen also for deuterium. But the compression rise is weaker than for D as seen in d) from the reduction of enrichment with pressure. A simple explanation for the enrichment behaviour may be given by the ratio of the impurity ionisation length versus the D ionisation length in the divertor, which is a measure for the entrainment of impurity flow in the D flow. The much higher ionization energy of Ne compared to Ar results in lower enrichment in the parameter range here. Other effects, as described in [53] [54] for the comparison of Ne and N may contribute as well for Ne as compared to Ar. In the analysed discharges of this paper, Ar is much better enriched in the divertor compared to Ne, but the effect is reduced at higher p_0 / lower divertor electron temperature (8 vs 15 eV) from the highest to lowest p_0. The overall higher enrichment of Ar makes it more suitable for divertor radiative cooling compared to Ne, also if cooling rates and dilution are taken into account.

5. Conclusions

Significant Ar radiation in the pedestal region is an actuator for shaping the pedestal pressure profile and thus may contribute to mitigation or avoidance of ELMs. Effects to be considered are the direct pressure variation via the electron heat flux reduction by impurity radiation, the effect of fuel ion dilution and Z_{eff} increase, changes in the edge bootstrap current and changes in transport in particular inside the pedestal top. In the type-I ELMy regime, the ELM size is moderately reduced and energy confinement is preserved or moderately increased. The electron pressure gradient is reduced close inside the separatrix, and increased inside the pedestal top. No significant trend of experimental and calculated critical pedestal pressure with the radiation level has been observed in a scan of heating power and Ar radiation at high plasma shaping. Therefore the improvement of energy confinement can be related to a reduction of turbulent transport inside the pedestal region, probably caused by the change of the pedestal

parameters further outside.

The combination of Ar seeding with a naturally ELM-free H-mode [17] can preserve the MHD modes responsible for ELM suppression and widens the operation window towards higher heating power and beta. Integration of Ar seeding with RMP ELM-supressed H-modes appeared promising, with no unfavourable Ar accumulation at the pedestal top. However, for an efficient power removal in devices like DEMO, operation at higher core/pedestal and divertor electron densities will be required. In general, the ELM-free regimes described above require a widening of the operational space towards a higher divertor neutral pressure to achieve simultaneously divertor detachment at higher power. This is the operational domain of small ELMs situated at high shaping, high gas puff levels and close to double null [55] [11]. Here, the additional transport required to avoid large ELMs is thought to be provided by ballooning modes close to the separatrix, which are also thought to be responsible for the small "ELMs" [11]. Integration of this regime with lower pedestal collisionality and radiative cooling inside the separatrix will be the subject of future studies.

Very small ELMs can be achieved with an X-point radiating zone situated a few cm above the X-point [25]. This regime is barely controllable via P_{sep} as determined by P_{heat}-$P_{radmain}$, since the sensor gets ill-conditioned due to the use of the difference of similarly large numbers with measurement uncertainties. In this case, control of the location of the X-point radiator [10] is favorable. Next steps will be refined tailoring of the pedestal pressure gradient including Kr and Xe radiation to extend the no-ELM parameter range and the integration with higher separatrix densities and divertor detachment at high power. For the latter, comparison of Ne and Ar injection revealed that Ar seems better suited for divertor radiative cooling than Ne due to its higher divertor enrichment. Evidence of entrainment of both Ne and Ar in the neutral D_2 flow was obtained, showing that neutral collisions between impurities and D_2 molecules will have to be taken into account in quantiative divertor modelling using engineering parameters as input. In view of its good prospects as a pedestal and divertor radiator, Ar should be considered as a prime candidate for integrated pedestal/divertor scenarios for DEMO, where Kr and Xe may provide further tailoring options for the pedestal heat flux distribution. For a precise prediction of the radiation profile in the pedestal, the neutral fuel density must be known due to its strong impact on the radiated power via its influence on the impurity ionization balance.

6. Acknowledgements

This work has been carried out within the framework of the EUROfusion Consortium and has received funding from the Euratom research and training programme 2014-2018 and 2019-2020 under grant agreement number 633053. The views and opinions expressed herein do not necessarily reflect those of the European Commission.

7. References

[1] WENNINGER, R. et al., Nucl. Fusion **57** (2017) 016011.
[2] ASAKURA, N. et al., Nucl. Fusion **57** (2017) 126050.
[3] WENNINGER, R. et al., Nucl. Fusion **54** (2014) 114003.
[4] FEDERICI, G. et al., Nucl. Fusion **59** (2019) 066013.
[5] SICCINIO, M. et al., Nucl. Fusion **59** (2019) 106026.
[6] PITTS, R. et al., Nuclear Materials and Energy **20** (2019) 100696.
[7] GOLDSTON, R. et al., Plasma Phys. Controlled Fusion (2017) 055015.
[8] KALLENBACH, A. et al., Plasma Physics and Controlled Fusion **58** (2016) 045013.
[9] KALLENBACH, A. et al., Nuclear Fusion **52** (2012) 122003.
[10] BERNERT, M. et al., X-point radiation, its control and an ELM suppressed radiating regime at the ASDEX Upgrade tokamak, submitted to Nuclear Fusion letters (2020).
[11] HARRER, G. et al., Nuclear Fusion **58** (2018) 112001.
[12] KALLENBACH, A. et al., Plasma Physics and Controlled Fusion **55** (2013) 124041.
[13] PÜTTERICH, T. et al., Nucl. Fusion **59** (2019) 056013.
[14] KALLENBACH, A. et al., Plasma Physics and Controlled Fusion **52** (2010) 055002.
[15] LUDA, T. et al., Nucl. Fusion **60** (2020) 036023.
[16] KALLENBACH, A. et al., Plasma Physics and Controlled Fusion **60** (2018) 045006.
[17] GIL, L. et al., Nucl. Fusion **60** (2020) 054003.
[18] GREENWALD, M. et al., Physics of Plasmas **6** (1999) 1943.
[19] MARTIN, Y. R. et al., Journal of Physics: Conference Series **123** (2008) 12033.
[20] VIEZZER, E., Nuclear Fusion **58** (2018) 115002.
[21] MEYER, H. et al., Nuclear Fusion **59** (2019) 112014.
[22] SUTTROP, W. et al., Plasma Physics and Controlled Fusion **46** (2004) A151.
[23] REINKE, M. et al., Nucl. Fusion **59** (2019) 046018.
[24] REINKE, M. et al., Invited Virtual Talk 62nd Annual Meeting of the APS Division of Plasma Physics, Nov 9-13, 2020.
[25] BERNERT, M. et al., Nuclear Materials and Energy **12** (2017) 111.
[26] XU, G. et al., Nucl. Fusion **60** (2020) 086001.
[27] WISCHMEIER, M. et al., J. Nucl. Mater. **463** (2015) 22.
[28] GLÖGGLER, S. et al., Nucl. Fusion **59** (2019) 126031.
[29] HUBER, A. et al., *Impact of strong impurity seeding on the radiation losses in JET with ITER-like wall*, in: Proc. of the 41th EPS Conference on Controlled Fusion and Plasma Physics, Berlin, Germany, http://ocs.ciemat.es/EPS2014PAP Huber P1.031.pdf, 2014.
[30] EVANS, T. et al., Phys. Rev. Lett. **92** (2004) 235003.
[31] SUTTROP, W. et al., Nuclear Fusion **58** (2018) 096031.
[32] MCDERMOTT, R. et al., Development of Ar^{16+} charge exchange recombination spectroscopy measurements at ASDEX Upgrade, submitted to Nuclear Fusion (2020).
[33] HU, Q. et al., Phys. Plasmas **26** (2019) 120702.
[34] HINSON, E. et al., Nucl. Fusion **60** (2020) 054004.
[35] DUX, R. et al., 'Effect of charge exchange on impurity radiation', submitted to Nuclear Fusion.
[36] MADDISON, G. et al., Nucl. Fusion **43** (2003) 49.
[37] LOARTE, A. et al., Phys. Plasmas **18** (2011) 056105.
[38] REINKE, M. et al., J. Nucl. Mater. **415** (2011) S340.
[39] PETRIE, T. et al., Nuclear Materials and Energy **19** (2019) 267.
[40] DUNNE, M. G. et al., Plasma Physics and Controlled Fusion **59** (2017) 025010.
[41] CAVEDON, M. et al., Nucl. Fusion **60** (2020) 066026.
[42] VIEZZER, E. et al., Review of Scientific Instruments **83** (2012) 103501.
[43] FISCHER, R. et al., Fusion Science and Technology **58** (2010) 675.
[44] TOKAR, M. Z. et al., Phys. Rev. Lett. **84** (2000) 895.

[45] DRENIK, A. et al., Nuclear Fusion **59** (2019) 046010.
[46] KALLENBACH, A. et al., Nuclear Materials and Energy **18** (2019) 166 .
[47] DUX, R. et al., Plasma Physics and Controlled Fusion **38** (1996) 989.
[48] KALLENBACH, A. et al., Nuclear Fusion **35** (1995) 1231.
[49] MCDERMOTT, R. M. et al., Plasma Physics and Controlled Fusion **60** (2018) 095007.
[50] DUX, R., Fusion Science and Technology **44** (2003) 708.
[51] ROHDE, V. et al., Journal of Nuclear Materials **390–391** (2009) 474.
[52] VAROUTIS, S. et al., Fusion Engineering and design **121** (2017) 13.
[53] GOETZ, J. et al., J. Nucl. Mater. **266-269** (1999) 354.
[54] SYTOVA, E. et al., Nuclear Materials and Energy **19** (2019) 72.
[55] STOBER, J. et al., Nuclear Fusion **41** (2001) 1123.